

Heterogeneous TiC-based composite ceramics with high toughness

Xiaoci Ma(马孝慈), Yufei Ge(葛雨非), Yutong Hou(侯语同), Keyu Shi(施柯羽), Jiaqi Zhang(张佳琪), Gaoping Yue(岳高平), Qiang Tao(陶强), and Pinwen Zhu(朱品文)

Citation: Chin. Phys. B, 2025, 34 (**8**): 086104. DOI: 10.1088/1674-1056/add5c8
http://cpb.iphy.ac.cn; http://iopscience.iop.org/cpb

What follows is a list of articles you may be interested in

Prediction of superionic state in LiH_2 at conditions enroute to nuclear fusion

Fude Li(李福德), Hao Wang(王豪), Jinlong Li(李津龙), and Huayun Geng(耿华运)
Chin. Phys. B, 2023, 32 (**10**): 106103. DOI: 10.1088/1674-1056/acea68

Dependence of nitrogen vacancy color centers on nitrogen concentration in synthetic diamond

Yong Li(李勇), Xiaozhou Chen(陈孝洲), Maowu Ran(冉茂武), Yanchao She(佘彦超), Zhengguo Xiao(肖政国), Meihua Hu(胡美华), Ying Wang(王应), and Jun An(安军)
Chin. Phys. B, 2022, 31 (**4**): 046107. DOI: 10.1088/1674-1056/ac3220

Synthesis, structure, and properties of $Ba_9Co_3Se_{15}$ with one-dimensional spin chains

Lei Duan(段磊), Xian-Cheng Wang(望贤成), Jun Zhang(张俊), Jian-Fa Zhao(赵建发), Li-Peng Cao(曹立朋), Wen-Min Li(李文敏), Run-Ze Yu(于润泽), Zheng Deng(邓正), Chang-Qing Jin(靳常青)
Chin. Phys. B, 2020, 29 (**3**): 036102. DOI: 10.1088/1674-1056/ab69ea

Polycrystalline cubic boron nitride prepared with cubic-hexagonal boron nitride under high pressure and high temperature

Ming Yang(杨鸣), Zi-Li Kou(寇自力), Teng Liu(刘腾), Jing-Rui Lu(卢景瑞), Fang-Ming Liu(刘方明), Yin-Juan Liu(刘银娟), Lei Qi(戚磊), Wei Ding(丁未), Hong-Xia Gong(龚红霞), Xiao-Lin Ni(倪小林), Duan-Wei He(贺端威)
Chin. Phys. B, 2018, 27 (**5**): 056105. DOI: 10.1088/1674-1056/27/5/056105

Behaviors of Zn_2GeO_4 under high pressure and high temperature

Shu-Wen Yang(杨淑雯), Fang Peng(彭放), Wen-Tao Li(李文涛), Qi-Wei Hu(胡启威), Xiao-Zhi Yan(晏小智), Li Lei(雷力), Xiao-Dong Li(李晓东), Duan-Wei He(贺端威)
Chin. Phys. B, 2016, 25 (**7**): 076101. DOI: 10.1088/1674-1056/25/7/076101

SPECIAL TOPIC — Structures and properties of materials under high pressure

Heterogeneous TiC-based composite ceramics with high toughness

Xiaoci Ma(马孝慈)[1,†], Yufei Ge(葛雨非)[2,†,‡], Yutong Hou(侯语同)[1], Keyu Shi(施柯羽)[1], Jiaqi Zhang(张佳琪)[1], Gaoping Yue(岳高平)[1], Qiang Tao(陶强)[1], and Pinwen Zhu(朱品文)[1,§]

[1] *Synergetic Extreme Condition High-Pressure Science Center, State Key Laboratory of High Pressure and Superhard Materials, College of Physics, Jilin University, Changchun* 130012, *China*

[2] *School of Materials Science and Engineering, Jilin Jianzhu University, Changchun* 130018, *China*

(Received 28 February 2025; revised manuscript received 28 April 2025; accepted manuscript online 8 May 2025)

Electrically conductive carbide ceramics with high hardness and fracture toughness are promising for advanced applications. However, enhancing both electrical conductivity and fracture toughness simultaneous is challenging. This study reports the synthesis of $(Ti_{0.2}W_{0.2}Ta_{0.2}Hf_{0.2}Mo_{0.2})$C-diamond composites with varying densities using high-pressure and high-temperature (HPHT) method. The carbides are uniformly dispersed in a titanium carbide matrix, forming conductive channels that reduce resistivity to 4.6×10^{-7} Ω·m. These composite materials exhibit metallic conductivity with a superconducting transition at 8.5 K. Superconducting behavior may result from d–p orbital hybridization and electron–phonon coupling in transition metal carbides, such as TaC, Mo_2C, and MoC. Optimizing intergranular bonding improves the fracture toughness without compromising hardness. The highest indentation toughness value is 10.1 ± 0.4 MPa·$m^{1/2}$, a 130% increase compare to pure TiC. Enhanced toughness arises from transgranular and intergranular fracture modes, multiple crack bridging, and large-angle crack deflection, which dissipate fracture energy and inhibit crack propagation. This study introduces a novel microstructure engineering strategy for carbide ceramics to achieve superior mechanical and electrical properties.

Keywords: high pressure and high temperature, hardness, fracture toughness, superconductivity

PACS: 61.50.–f, 61.72.U–, 62.20.–x, 61.66.Fn

DOI: 10.1088/1674-1056/add5c8 **CSTR:** 32038.14.CPB.add5c8

1. Introduction

Titanium carbide (TiC)-based ceramics possess a distinctive combination of mechanical, chemical, and physical properties, such as ultra-high temperature resistance, exceptional hardness, superior wear resistance, outstanding corrosion resistance, and excellent conductivity. These materials play a crucial role in the domain of engineering applications, including advanced technologies like shield machine cutterheads, gas rudders, nozzle liners, turbine blades, and structural building materials for nuclear reactors.[1–3] However, their relatively low toughness poses a significant challenge to both mechanical processing and service life in extreme conditions.[4,5] The development of TiC-based composite materials with enhanced toughness can significantly improve their suitability for extreme working environments and high-impact applications.

The toughening of TiC-based materials generally entails incorporating toughening phases during the sintering process to suppress crack nucleation and enhance crack deflection capabilities, thereby achieving improved toughness.[6,7] Conventional high-toughness materials can primarily be categorized into two types. First, metals achieve exceptionally high fracture toughness by inducing dislocation slip.[8] However, composite metals may significantly compromise the material's hardness. Second, high-toughness ceramics, like Si_3N_4, promote stress passivation and relaxation at the crack tip via mechanisms like crack deflection and crack bridging.[9] However, the integration of the aforementioned materials is likely to impair conductivity owing to the insulating properties inherent in the precursor.[10–12] Therefore, achieving the enhancement and toughening of TiC while preserving its exceptional hardness and conductivity represents a significant research focus in TiC-based ceramics. At present, strong and tough composite materials are primarily enhanced by incorporating tough phases such as ZrC,[10] SiC,[11] and Al_2O_3-ZrO_2.[12] For instance, Yung *et al.*[10] investigated the toughening effect of ZrC in TiC-based composites. Cheng *et al.*[11] developed a hard composite material with high toughness by inducing crack deflection by the addition of silicon carbide grains to TiC. Zhu *et al.*[12] prepared TiC-based composite ceramics with ultra-high toughness using Al_2O_3 and ZrO_2. These composite materials exhibit superior fracture resistance compared to pure TiC ceramics. However, this strategy inevitably introduces trade-offs in properties such as hardness and con-

[†]These authors contributed equally to this work.

[‡]Corresponding author. E-mail: geyufei@jlju.edu.cn

[§]Corresponding author. E-mail: zhupw@jlu.edu.cn

© 2025 Chinese Physical Society and IOP Publishing Ltd. All rights, including for text and data mining, AI training, and similar technologies, are reserved.

ductivity. Therefore, selecting appropriate second-phase materials and optimizing preparation methods are crucial factors for achieving conductive TiC-based composites that possess high toughness and high hardness.

Achieving enhanced fracture toughness while maintaining high hardness and conductivity remains a formidable challenge in TiC-based composites. One promising strategy involves the dispersion of various carbides within a TiC matrix to construct heterostructures. A potential pathway for enhancing toughening in TiC can be offered by these heterostructures, which facilitate diverse crack propagation pathways through altering the strength of different phases.[13] Furthermore, incorporating carbides with comparable conductivity during composite synthesis enables precise optimization of electronic transport characteristics post-sintering, which is advantageous for achieving excellent conductivity. In conventional solid-phase synthesis, metal elements influence carbides to exhibit different growth rates, which may impair both mechanical and electrical properties of multiphase composites. Compared with traditional solid reactions, densification can be achieved at lower temperatures (such as 1400–1600 °C) by reducing the atomic diffusion activation energy under high pressure, which alleviates the abnormal grain growth caused by prolonged high-temperature sintering. The high-pressure and high-temperature (HPHT) method has proven effective in refining grain structures and inducing deformation that fills vacancies between grains, resulting in the densification of carbide composites.[14] Meanwhile, pressure serves as an effective means to regulate the microstructure of grains, which can form rich crack blunting modes and high fracture toughness.

In this work, heterogeneous carbides-composites with a TiC matrix were synthesized using HPHT method. The materials obtained at different temperatures were characterized through electron microscopy, hardness tests, and electrical measurements. The HPHT method is conducive to constructing heterostructures for TiC-based composite materials with high electrical conductivity, high hardness, and high toughness. Multifunctional TiC-based composite materials provide a promising path for expanding their potential applications in fields such as armor protection and biological support.

2. Experiment

2.1. Sample synthesis

The preparation of the composite material was carried out using a HPHT method. Information on precursors can be found in Table 1. TiC, WC, TaC, HfC, Mo_2C, and nanodiamond powders were ground for 2 h at a molar ratio of 2:2:2:2:1:10 to achieve a homogeneous mixture in an agate mortar. Energy-dispersive x-ray spectroscopy (EDS) confirmed the absence of silicon contamination in the mixed powder (as shown in Fig. S1). The resulting samples were designated HEC-1, HEC-2, HEC-3, HEC-4, and HEC-5, in accordance with the different sintering temperatures. The mixed powders were compacted into cylindrical samples with a diameter of 4 mm and a height of 2 mm using a mold under a pressure of 100 MPa.

Table 1. Information related to precursors.

Name	State	Size (μm)	Purity (%)	Producer
Titanium carbide	powder	2.0–4.0	99.99	Shanghai Aladdin Biochemical Technology Co., Ltd, China
Tungsten carbide	powder	10.0	99.99	Shanghai Aladdin Biochemical Technology Co., Ltd, China
Hafnium carbide	powder	0.4	99.9	Shanghai Aladdin Biochemical Technology Co., Ltd, China
Molybdenum carbide	powder	2.0–4.0	99	Shanghai Aladdin Biochemical Technology Co., Ltd, China
Tantalum carbide	powder	3.0	99.5	Shanghai Aladdin Biochemical Technology Co., Ltd, China
Diamond	powder	0.1	99	Henan Zhongyuan Diamond Co., Ltd, China

HPHT method was conducted for 30 min at temperatures ranging from 1000 °C to 1800 °C and a pressure of 5.0 GPa, using a cubic anvil HPHT apparatus (SPD-6 × 14400 kN, Guilin Guiye Heavy Industry Co., Ltd. China). Select pressure calibration materials with phase transition points above 2.0 GPa and phase transitions accompanied by a sudden change in resistance: Bi (phase transition points of 2.55 GPa for I–II, 2.69 GPa for II–III), Tl (phase transition point of 3.68 GPa), and Ba (phase transition point of 5.5 GPa).[15] Variation of sample resistance with oil pressure was tested using the two-wire method. The pressure calibration assembly was 4 mm assembly. For the standard compression 4 mm sample assembly, a graphite heater was used. Temperature was measured using W–Re-type thermocouples, and pressure was estimated from previously obtained calibration curves for the cubic-anvil, high-pressure apparatus. The recovered samples were 4 mm in diameter and 2 mm in height, which were then polished for further analysis.

2.2. Sample characterization

The structures of the recovered samples were characterized using x-ray diffraction (XRD, R-AXIS-RAPID II, Rigaku, Japan) with Cu $K\alpha$ radiation ($\lambda = 1.5418$ Å). Raman spectroscopy of the samples has been supplemented. Raman spectra were obtained to analyze samples, and the samples were excited using a 532 nm laser (Nd-YAG 532 nm).

The fracture surfaces and indentations were examined using scanning electron microscopy (SEM, FEI Magellan 400 L).

Vickers hardness measurements were performed using microhardness testers (HMAS-D1000SMZC, HMAS-D5SMZC). The Vickers hardness was determined as

$$H_{\mathrm{V}} = k\frac{F}{S} = 1854.4 \times \frac{F}{L^2}, \tag{1}$$

where F (N) is the applied load and L (μm) is the average diagonal length of the Vickers indentation.[16,17] The indentation toughness was calculated as

$$K_{\mathrm{IC}} = 0.016 \times \frac{E^{0.5}F}{H_{\mathrm{V}}^{0.5}C^{1.5}}, \tag{2}$$

where C is the average length of the radial cracks measured from the indent center, and E is the Young's modulus of the samples. The toughness of all samples was calculated at an applied load of 9.8 N.[18] The Young's modulus E was measured using a Nano Indenter (G200, Keysight). E of the test material was calculated using

$$\frac{1}{E_{\mathrm{r}}} = \frac{1-\nu^2}{E} + \frac{1-\nu_{\mathrm{i}}^2}{E_{\mathrm{i}}}, \tag{3}$$

$$E_{\mathrm{r}} = \frac{\sqrt{\pi}\cdot S}{2\beta\sqrt{A}}, \tag{4}$$

where ν is the Poisson's ratio of the test material ($\nu = 0.10$), E_{i} and ν_{i} are the Young's modulus and Poisson's ratio, respectively, of the indenter ($E_{\mathrm{i}} = 1141$ GPa and $\nu_{\mathrm{i}} = 0.07$), β is a constant that depends only on the geometry of the indenter ($\beta = 1.034$), A is the projected contact area at that load, and S is the slope of the initial portion of the unloading curve.[19,20]

Room-temperature resistivity was determined via the van der Pauw method with four-point probe configuration. Electrical transport and magnetic property measurements were carried out using a physical property measurement system (PPMS, Quantum Design). Cuboid blocks of the sample measuring 3 mm×0.5 mm×0.5 mm was prepared for wire attachment to measure resistivity from 2 K to 300 K employing the four-probe method. Bulk density was quantified through Archimedes' principle using anhydrous ethanol as the immersion medium.

3. Result and discussion

3.1. XRD analysis

The XRD patterns of five samples synthesized under varying temperatures are illustrated in Fig. 1. The diffraction profiles confirm the presence of multiple carbide phases, including TiC, WC, TaC, HfC, and Mo_2C. Notably, no distinct diamond peaks corresponding to (111) or (220) were observed due to overlap with dominant carbide reflections from the carbide phases (Fig. 1). Below 1600 °C, the phase composition remained predominantly characterized by the initial carbides. However, elevated temperatures induced a phase transformation of Mo_2C, as evidenced by the intensity attenuation of the characteristic peak at 39.8° (Fig. 1). Moreover, the peak at 26.5° corresponds to graphite at 1800 °C, indicating progressive diamond graphitization under extreme thermal conditions.[21] These observations collectively demonstrate that high-temperature sintering promotes carbon redistribution under high pressure. The presence of graphitized diamond provides an excess of carbon, which promotes the formation of other molybdenum carbide phases while simultaneously suppressing the metastable Mo_2C phases. Appropriate graphitization (formation of sp^2-hybridized carbon) can significantly enhance electrical conductivity, while excessive graphitization may disrupt the carbide matrix structure, thereby compromising both electrical conductivity and hardness.

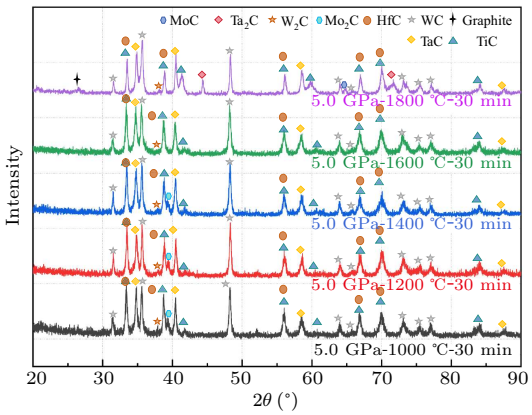


Fig. 1. XRD patterns of five samples recovered from different conditions indicated by T (in °C) pairs.

3.2. Mechanical mechanism and density

To characterize the mechanical properties of $(Ti_{0.2}W_{0.2}Ta_{0.2}Hf_{0.2}Mo_{0.2})C$-diamond composites, we measured bulk density and Vickers hardness. Figure 2(a) shows the convergent Vickers hardness under an applied load of 500 g. As depicted in Fig. 3(c), the hardness increased from 14.87 ± 0.12 GPa (HEC-1, 1000 °C) to a peak of 22.15 ± 0.08 GPa (HEC-4, 1600 °C), then dropped sharply to 18.52 ± 0.21 GPa at 1800 °C (HEC-5). This trend correlates with densification dynamics (Fig. 3(a)): density increased from 10.64 ± 0.12 g/cm^3 (HEC-1) to 12.71 ± 0.14 g/cm^3 (HEC-4) below 1600 °C, but subsequently decreased to 11.2 ± 0.09 g/cm^3 at 1800 °C. The initial hardness increase is due to pore reduction through high-pressure intergranular compaction, where softer carbide phases (e.g., Mo_2C) occupy voids between TiC/WC grains. Beyond 1600 °C, accelerated grain growth led to localized hard-phase agglomeration (e.g., HfC, TaC), creating stress-concentration sites that adversely affected both density and hardness.[22]

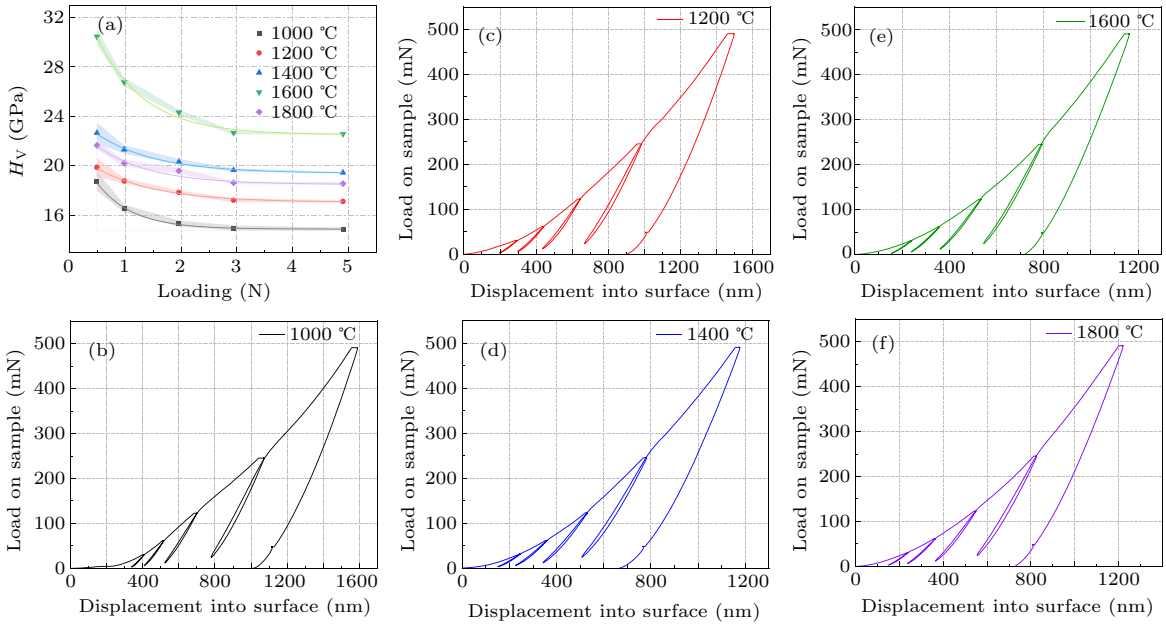


Fig. 2. Mechanical test results of five samples recovered from different conditions. (a) Vickers hardness test results of five synthesized samples recovered from different conditions indicated by T (in °C) pairs. (b)–(f) Loading and unloading curves of indentation tests for five synthesis samples recovered from different conditions indicated by T (in °C) pairs.

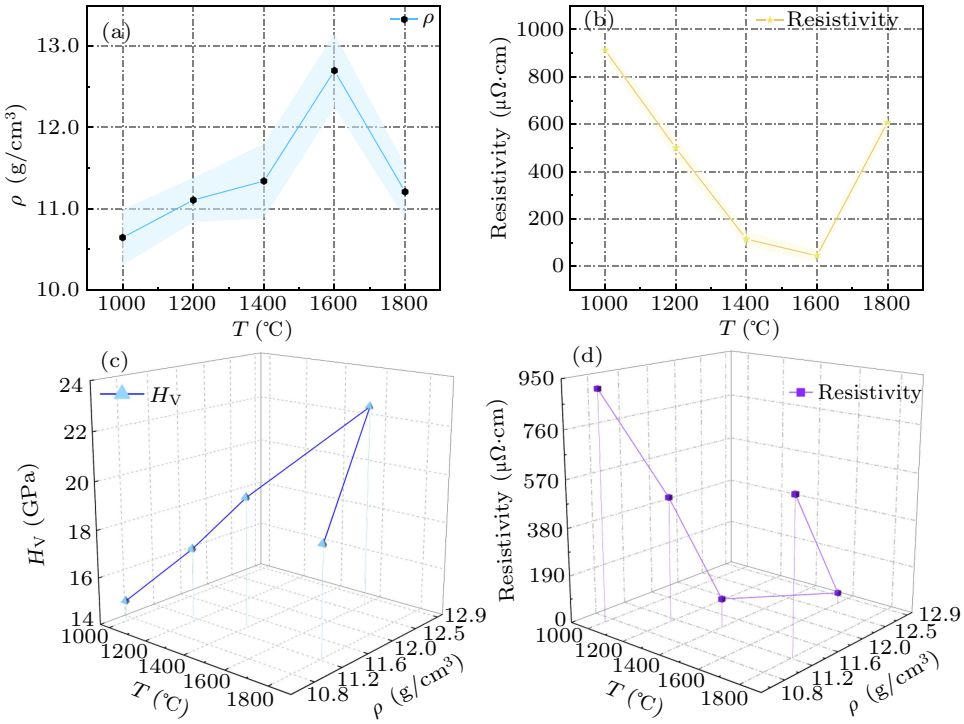


Fig. 3. Other physical properties of five samples recovered from different conditions indicated by T (in °C) pairs. (a) Density results of five synthesized samples recovered from different conditions indicated by T (in °C) pairs. (b) Resistivity results of five synthesized samples recovered from different conditions indicated by T (in °C) pairs. (c) Trend of the relationship between Vickers hardness, density, and temperature. (d) Trend of the relationship between resistivity, density, and temperature.

The high hardness of the sample originates from the presence of various carbide phases that fill the interstitial regions between the high-hardness TiC grains. This not only effectively reduces porosity but also enhances the sintering sintering densification.[23] Additionally, the uniform dispersion of TiC grains forms a robust hard matrix, which serves as a critical basis for achieving high hardness.[24] To further understand the hardness mechanism of $(Ti_{0.2}W_{0.2}Ta_{0.2}Hf_{0.2}Mo_{0.2})$C-diamond composites, Young's modulus measurements were conducted on the composites samples. Young's modulus quantifies the resistance of solid materials to elastic deformation.[25] The values of Young's modulus were determined via nanoindentation testing, yielding maximum values of 204 GPa, 217 GPa, 356 GPa, 381 GPa, and 326 GPa for HEC-1, HEC-2, HEC-3, HEC-4, and HEC-5, respectively. Young's modulus measurements via nano-

indentation (Figs. 2(b)–2(f)) further supported these findings. Notably, HEC-4 exhibited the highest modulus (381 GPa), whereas HEC-1 displayed the lowest value (204 GPa). The strong correlation among Young's modulus, hardness, and density underscores that optimal sintering at 1600 °C minimizes porosity while maintaining a fine-grained microstructure.

The Vickers indentation toughness (K_{IC}) of the synthesized samples was measured. The sample exhibiting the most comprehensive mechanical properties was synthesized under experimental conditions of 5.0 GPa and 1600 °C. The calculated K_{IC} value attained is 10.1 ± 0.4 MPa·m$^{1/2}$, as determined by the Vickers indenter with a load of 9.8 N, which is almost 2.3 times greater than that of TiC (4.3 MPa·m$^{1/2}$).[26] Due to the limited size of the sample, it is challenging to prepare reliable CNB experimental samples. Consequently, the indentation method, which is well-suited for small-sized samples, was employed to evaluate the toughness of the samples.

SEM was employed to characterize the cracks in the samples exhibiting optimal toughness (HEC-4), thereby deepening understanding of the toughening mechanisms involved. As shown in Fig. 4(a), HEC-4 demonstrates a variety of toughening mechanisms, including the interplay between transgranular fracture (TF) mode and intergranular fracture (IF) mode, multiple cracks bridging, and large-angle deflection of cracks. Crack propagation typically follows the path that minimizes energy dissipation. It is noteworthy that the grain boundary strength in polycrystalline materials tends to be relatively low. Consequently, the IF mode is identified as the predominant fracture mechanism in polycrystalline materials. The mixed-mode fracture observed in HEC-4 (Fig. 4(b)) indicates that the presence of high-strength grain boundaries forces cracks to propagate within the grains. The combination of IF and TF modes in HEC-4 enables a greater dissipation of fracture energy compared to the sole occurrence of the IF mode.[27] In addition, Fig. 4(b) illustrates that the interaction between IF and TF modes in HEC-4 can generate large angle crack deflection. The presence of multiphase carbides causes induced cracks to deviate from their original trajectories, thereby reducing the stress concentration at the crack tip and providing a shielding effect against crack propagation.[28,29] In Fig. 4(c), multiple cracks bridging was observed in HEC-4. Furthermore, intermittent crack propagation occurred during the process of crack propagation in grains. This phenomenon reveals mechanisms of multiple crack nucleation and multi-stage bridging toughening. Influenced by this special mode of crack propagation, a stepped deflection pattern was achieved in the grain structure. The occurrence of multiple crack nucleation effectively dissipates fracture energy and mitigates stress at the crack tip[30,31] throughout the propagation process. Additionally, multiple bridge connections effectively link both sides of the crack, inhibiting further crack propagation. These mechanisms are controlled by a heterogeneous microstructure combining a rigid TiC matrix with dispersed other carbides, where structural and strength difference synergistically induce special crack propagation, thereby enhancing fracture toughness.

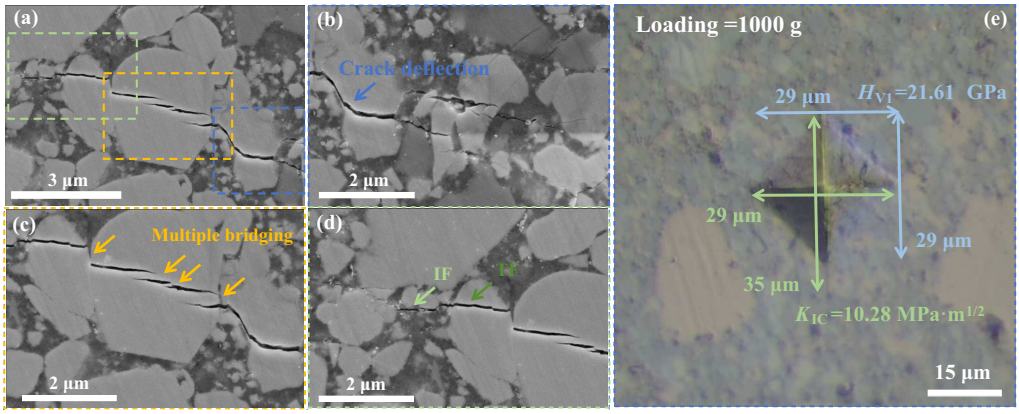


Fig. 4. Typical toughening mechanisms in the HEC-4. (a) SEM image of the crack propagating in the HEC-4. The blue dashed area shows crack deflection. The yellow dashed area shows multiple bridging. The green dashed area shows transgranular fracture (TF) mixed with intergranular fracture (IF). (b) SEM image of microstructure of crack deflection, corresponding to the blue-boxed area in (a). (c) SEM image of multiple bridging, corresponding to the yellow-boxed area in (a). (d) SEM image of TF mixed with IF, corresponding to the green-boxed area in (a). (e) Vicker indentation with a load of 9.8 N.

3.3. Resistivity and superconductivity

The constituent carbides exhibit metallic conduction characteristics, with electrical resistivities of 2.2×10^{-7} Ω·m for WC,[32] 3.7×10^{-7} Ω·m for HfC,[33] 4.2×10^{-7} Ω·m for TaC,[34] and 6.8×10^{-7} Ω·m for TiC.[26] Conventional TiC-based composites often suffer from conductivity degradation due to insulating toughening phases, limiting their industrial utility. Remarkably, the $(Ti_{0.2}W_{0.2}Ta_{0.2}Hf_{0.2}Mo_{0.2})C$-diamond composites (HEC-4, Table 2) exhibit a minimum resistivity of 4.6×10^{-7} Ω·m, comparable to monolithic TiC. This performance stems from two synergistic factors. High-pressure sintering produces dense heterostructures with per-

colative carbide networks, and partial diamond graphitization at 1600 °C introduces conductive sp^2-hybridized carbon pathways.[21] As shown in Fig. S3, the Raman spectra of the samples synthesized under conditions of 5.0 GPa and 1400 °C exhibit a pronounced graphite G peak. With increasing temperature ($\geq$ 1600 °C), the D and G vibration modes of graphite become increasingly prominent. These Raman spectroscopy results confirm the reliability of the diamond graphitization process in HEC-4. A strong positive correlation exists between density and conductivity (Fig. 3(d)). Below 1600 °C, resistivity increased with temperature (Fig. 3(b)) due to limited graphitization preserved insulating diamond domains. Above 1600 °C, resistivity decreased due to enhanced sp^2 carbon content. However, excessive graphitization at 1800 °C disrupted grain boundary connectivity, leading to an elevated resistivity of 6.0×10^{-6} Ω·m (HEC-5).[36]

Table 2. Information of various carbide materials, hardness test load is 29.4 N.

Name	Hardness (GPa)	Fracture toughness (MPa·m$^{1/2}$)	Resistivity (μΩ·cm)
WC(CO)[32]	15.8	8.1–14.5	22
HfC[33]	18.25		37
TiC[26]	28	4.3	40
TaC[34]	15.7	3.4–6.6	25
Mo_2C[35]	15.9–16.3	3.9–5.0	
This work	20.02	10.1	46

The electronic transport behavior of HEC-4 was investigated at low temperatures using the four-probe method. As shown in Fig. 5(a), the temperature-dependent resistivity (ρ–T) curve reveals a room-temperature resistivity of $\sim 10^{-7}$ Ω·m at 300 K, comparable to platinum under ambient conditions. Resistivity decreases monotonically with cooling, indicating characteristic metallic behavior likely due to conduction channels formed within the TiC matrix. An abrupt resistivity drop at 8.5 K marks the onset of superconductivity with a critical temperature (T_c) of 8.5 K. Complementary magnetization versus temperature measurements (Fig. 5(b)) confirm this transition, where the magnetization exhibits a pronounced drop to significant diamagnetism below 8.5 K. Regrettably, zero resistance and complete diamagnetism were not observed at 2 K, which can be attributed to the broadening of the superconducting transition width (ΔT_c). The widening of ΔT_c indicates that superconductivity in the sample is sensitive to impurities such as grain boundaries.[37,38] This also demonstrates that the HPHT method facilitates the combination of superconducting phases at grain boundaries during growth. The superconducting properties of HEC-4 are related to superconducting tantalum carbide and molybdenum carbide, such as TaC, Mo_2C, and MoC.[39–41] The hybridization of d orbitals and p orbitals of C atoms have played an important role in the conductivity and superconductivity of these transition metal carbides. Noffsinger *et al.*[39] proposed that the predominant d-electrons of Ta at the Fermi level leads to an increase in the density of electronic states, which is closely related to the electron–phonon coupling of superconductivity. Additionally, the Fermi surface of TaC exhibits weak nesting effects, which may facilitate the formation of superconducting Cooper pairs. Ge *et al.*[40] pointed out that in Mo_2C, the d orbitals of Mo hybridize with the p orbitals of C, which facilitates the formation of Cooper pairs. Separately, Kavitha *et al.*[41] demonstrated the presence of a deep pseudo gap at the Fermi level in MoC, indicating the possibility of superconductivity in its stable phase. HEC-4 of the composite phase in this study exhibits a single superconducting transition temperature of 8.5 K, which is more closely aligned with that of MoC and TaC. This suggests the presence of more complex cooperative superconductivity, requiring further comprehensive and systematic investigation in future studies. Consequently, this composite method not only improves the electrical conductivity of TiC-based ceramics but also induces superconducting behavior in this material, making it suitable for use under extreme superconducting conditions.

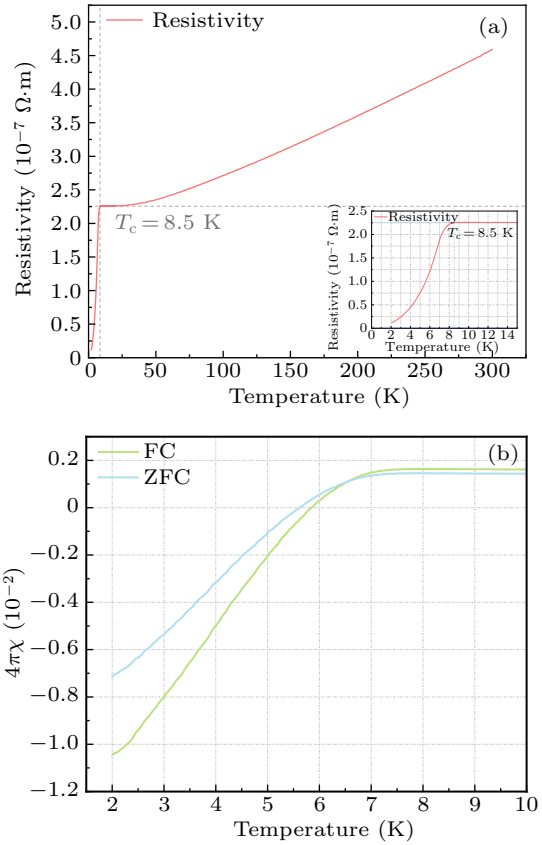


Fig. 5. The testing results of the physical property measurement system (PPMS). (a) The temperature dependence of resistivity (ρ–T) curve of HEC-4. The inset shows the localized magnified image near T_c. (b) The temperature dependence of field-cooling magnetization (green) and zero-field cooling magnetization (blue) curves of HEC-4.

3.4. Microstructure analysis

SEM was employed to systematically investigate the fracture surface morphology and grain size evolution across different sintering temperatures. Figures 6(a), 6(c), 6(e), 6(g), and

6(i) present the temperature-dependent microstructural development in sintered specimens. EDS mapping revealed homogeneous spatial distributions of carbon and titanium elements among carbide grains, suggesting effective elemental intermixing. This promotes robust intergranular bonding networks between grains within the composite matrix. Below 1800 °C, minimal grain growth occurred due to insufficient thermal activation energy. Notably, TaC grains demonstrated better refinement capabilities under these conditions.[42] The resulting microstructure features a continuous TiC matrix phase with secondary carbide components uniformly distributed throughout. An interconnected TiC network establishes continuous conduction pathways, significantly contributing to electrical conductivity enhancement. Below 1600 °C, improved conductivity correlates with enhanced TiC matrix continuity. Above this threshold, diamond graphitization initiates, generating additional carbon-based conductive channels. The dual conduction mechanism combining TiC matrix and graphitic carbon explains the observed conductivity maximum occurring at intermediate temperatures. However, as the temperature rises further, excessive grain growth intensifies and severe diamond graphitization occur. At 1800 °C, excessive grain growth weakens inter-grain, increasing pore formation and reducing both mechanical properties and conductivity.

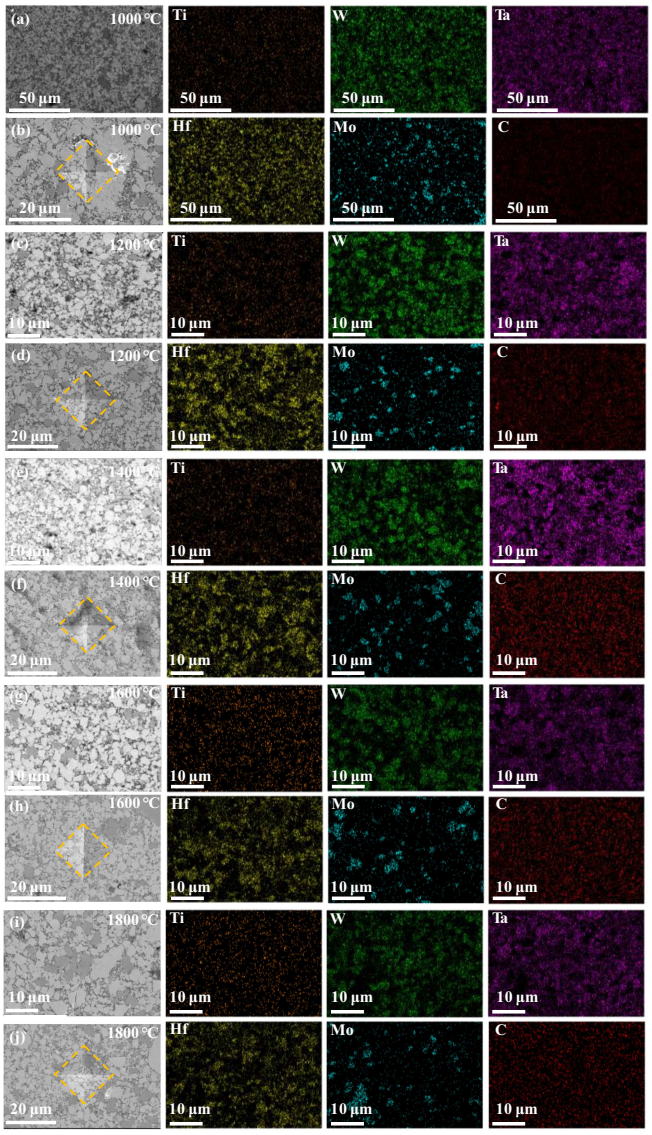


Fig. 6. SEM images of HEC-1, HEC-2, HEC-3, HEC-4 and HEC-5. (a), (c), (e), (g), (i) SEM images and corresponding EDS mapping showing the elements distribution in the polished surface of sample HEC-1, HEC-2, HEC-3, HEC-4 and HEC-5 after sintering at different temperature for 30 min; EDS mapping analysis: C element (red), Ti element (orange), Hf element (yellow), Ta element (purple), W element (green), and Mo element (blue). (b), (d), (f), (h), (j) SEM indentation images of sample HEC-1, HEC-2, HEC-3, HEC-4 and HEC-5 after sintering at different temperature for 30 min.

The mechanical and electrical properties of the synthesized composites display a non-monotonic temperature dependency, with a peak observed at 1600 °C (Figs. 3(c) and 3(d)). This behavior underscores the critical role of heterostructure-driven densification in balancing multifunctionality. As shown in Table 2, HEC-4 achieved extremely high fracture toughness and excellent conductivity without significantly sacrificing hardness.

4. Conclusion

TiC-based carbide composites were synthesized using the HPHT method, achieving unprecedented multifunctionality. HEC-4 achieves an indentation toughness of 10.1 MPa·m$^{1/2}$, a 130% increase over pure TiC due to TF/IF mode interactions and crack deflection/bridging mechanisms. The optimal hardness is 22.15 GPa, attributed to HPHT-induced densification. Metallic conductivity reaches 4.6×10^{-7} Ω·m through carbide networks and sp^2-carbon pathways formed during densification. Superconductivity emerges below 8.5 K, correlating with d–p orbital hybridization and electron–phonon coupling in transition metal carbides such as TaC, Mo_2C, and MoC. This study provides a strategy for developing heterogeneous ceramic with high toughness, conductivity, and superconductivity, and paves the way for superconducting applications under extreme conditions.

Acknowledgements

The authors acknowledge “B1 station, Synergetic Extreme Condition User Facility (SECUF)” for all of high-pressure experiments. The authors acknowledge funding support from the Science and Technology Development Project of Jilin Province (Grant No. SKL202402004), the Program for the Development of Science and Technology of Jilin Province (Grant No. YDZJ202201ZYTS308), and the Open Research Fund of State Key Laboratory of Inorganic Synthesis and Preparative Chemistry (Jilin University, Grant Nos. 2022-16 and 2022-23).

References

[1] Wan J S, Chen Y, Huang C J, Huang Z J, Liang C, Deng X L and Cheng Q F 2024 *Nature* **634** 1103
[2] Cho Y, Park J, Lee W G, Park J, Shin K, Song I, Lee G, Cho J, Kang S J, Kim Y, Baek M J and Lee D W 2023 *Adv. Funct. Mater.* **33** 2213853
[3] Xu S, Wang T, Wang X G, Wu L, Fang Z Q, Ge F F, Meng X, Liao Q, Wei J C and Li B S 2023 *Chin. Phys. B* **32** 068102
[4] Yue Y H, Gao Y F, Hu W T Xu B, Wang J, Zhang X J, Zhang Q, Wang Y B, Ge B H, Yang Z Y, Li Z H, Ying P, Liu X X, Yu D L, Wei B, Wang Z C, Zhou X F, Lin G and Tian Y J 2020 *Nature* **582** 370
[5] Fan J Z, Shen W X, Zhang Z F, Fang C, Zhang Y W, Chen L C, Wang Q Q, Wan B and Jia X P 2021 *Chin. Phys. B* **30** 038105
[6] Tong S, Ma Z C, Zhang W, Li Y C, Li C F, Zhao H W, Ren L Q and Yan C L 2024 *Small* **20** 2406042
[7] Gao J, Bai Y L, Fan H L, Song G P, Zou X C, Zheng Y T and He X D 2023 *J. Am. Ceram Soc.* **106** 4877
[8] Jiang W T, Lu H, Chen J H, Luo L, Liu X M, Wang H B and Song X Y 2023 *ACS Appl. Mater. Interfaces* **15** 19604
[9] Ritchie R O 2011 *Nat. Mater.* **10** 817
[10] Yung D L, Kollo L, Hussainova I and Žikin A 2013 *Key Eng. Mater.* **527** 20
[11] Cheng L X, Xie Z P and Liu G W 2013 *Ceram. Int.* **39** 5077
[12] Zhu Y B, Chai J L, Shen T L and Wang Z G 2021 *Metall. Mater. Trans. A* **52** 767
[13] Zhao H Z, You Z S, Tao N R and Lu L 2022 *Acta Mater.* **228** 117748
[14] Sun Y, Bai X F, Guo R F and Shen P 2025 *J. Mater. Sci. Technol.* **210** 188
[15] Onodera A and Ohtdni A 1998 *J. Appl. Phys.* **51** 2581
[16] Chaudhri M M 2020 *Diam. Relat. Mater.* **109** 108076
[17] Sagar K G and Suresh P M 2018 *AIP Conf. Proc.* **2039** 020073
[18] Shen X L, Wu K P, Sun H Y, Sang L W, Huang Z H, Imura M, Koide Y, Koizumi S and Liao M Y 2021 *Diam. Relat. Mater.* **116** 108403
[19] Pharr G M and Oliver W C 1992 *J. Mater. Res.* **7** 1564
[20] Gibmeier J and Scholtes B 2008 *Mater. Sci. For.* **571–572** 83
[21] Liu J, Zhan G D, Wang Q, Yan X Z, Liu F M, Wang P, Lei L, Peng F, Kou Z L and He D W 2018 *Appl. Phys. Lett.* **112** 061901
[22] Cui S W, Ge Y F, Ma S L, Zhang X Q Lian M, Wei X M, Li W, You C, Tao Q, Cui T and Zhu P W 2025 *J. Eur. Ceram. Soc.* **45** 116953
[23] Wang C C and Song L L 2019 *Chin. Phys. B* **28** 066201
[24] Tan C L, Ziu J, Wang D, Ma W Y and Zhou K S 2022 *Compos. Part B-Eng.* **236** 109820
[25] Yuan X H, Chen G W, Cheng Y, Zhu S C, Liu F Y, Ke Y J, Hu K, Pan Y, Wang M S, Liu Z D, Tang H and Liu B B 2025 *Sci. Bull.* **70** 1257
[26] Hu J L, Liu X, Hu C Y and Guo W M 2013 *China Ceram.* **49** 1 (in Chinese)
[27] Lian M, Wang F, Rong K X, Ma X C, Liu H T, Gai X M, Ge Y F, Dong S S, Tao Q and Zhu P W 2024 *Int. J. Refract. Met. H.* **118** 106490
[28] Lai S L, Zang J H, Shen W X, Huang G F, Chao F, Zhang Y W, Chen L C, Wang Q Q, Wan B, Jia X P and Zhang Z F 2023 *J. Eur. Ceram. Soc.* **43** 3090
[29] Wang H, Zhao Q Y, Xin S W, Zhao Y Q, Zhou W and Zeng W D 2021 *Mater. Sci. Eng. A* **821** 141626
[30] Qiu K L, Hou J P, Chen S, Li X, Yue Y H, Xu B, Hu Q, Liu L M, Yang Z Y, Nie A, Gao Y F, Jin T Y, Wang J, Li Y H, Wang Y B, Tian Y J and Guo L 2023 *Nat. Mater.* **22** 1317
[31] Xu K, Fang T, Zhao L F, Cui H C and Lu F G 2020 *Acta Metall. Sin.* **33** 425
[32] Williams W S 1999 *Int. J. Refract. Met. H.* **17** 21
[33] Liu J X, Kan Y M and Zhang G L 2010 *J. Am. Ceram. Soc.* **93** 980
[34] Silvestroni L, Pienti L, Guicciardi S and Sciti D 2015 *Comp. Part B* **72** 10
[35] Liang H, He R Q, Liu L, Zhang W and Fang L M 2023 *Ceram. Int.* **49** 7341
[36] Yu X L, Zhou X K, Wu B Z, Shi B C, Mi Y W, Yu Z X Jin Z H, Zhao Z N, He B Y, Chen H, Zheng Y F and Ge L 2024 *Ceram. Int.* **50** 40216
[37] Karki A B, Xiong Y M and Haldolaarachchige N, Stadler S, Vekhter I, Adams P W, Young D P, Phelan W A and Chan J Y 2011 *Phys. Rev. B* **83** 144525
[38] Arima K, Matano K, Harada S Bao G Z, Inada Y and Zheng G Q 2013 *J. Phys. Conf. Ser.* **449** 012034
[39] Noffsinger J, Giustino F, Louie S G and Cohen M L 2008 *Phys. Rev. B* **77** 180507
[40] Ge Y F, Song H, Bao K, Ma S L, Li L, Tao Q, Zhu P W, Liu B, Duan D F and Cui T 2021 *J. Alloy Compd.* **881** 160631
[41] Kavitha M, Sudha Priyanga G and Rajeswarapalanichamy R and Iyakutti K 2016 *Mater. Chem. Phys.* **169** 71
[42] Wang J W, Zhang Z G, Liang H and Chen H H 2021 *Chin. J. High Pre. Phys.* **35** 021101